

All-optical single-shot readout of a superconducting qubit

Georg Arnold^{*,†}, Thomas Werner^{*}, Rishabh Sahu, Lucky N. Kapoor, Liu Qiu, and Johannes M. Fink[‡]
Institute of Science and Technology Austria, Am Campus 1, 3400 Klosterneuburg, Austria

(Dated: October 26, 2023)

The rapid development of superconducting quantum hardware is expected to run into significant I/O restrictions due to the need for large-scale error correction in a cryogenic environment [1, 2]. Classical data centers rely on fiber-optic interconnects to remove similar networking bottlenecks and to allow for reconfigurable, software-defined infrastructures [3]. In the same spirit, ultra-cold electro-optic links [4] have been proposed [5] and used to generate qubit control signals [6], or to replace cryogenic readout electronics. So far, the latter suffered from either low efficiency [7], low bandwidth and the need for additional microwave drives [8], or breaking of Cooper pairs and qubit states [9]. In this work we realize electro-optic microwave photonics at millikelvin temperatures to implement a radio-over-fiber qubit readout that does not require *any* active or passive cryogenic microwave equipment. We demonstrate all-optical single-shot-readout by means of the Jaynes-Cummings nonlinearity [10] in a circulator-free readout scheme. Importantly, we do not observe any direct radiation impact on the qubit state as verified with high-fidelity quantum-non-demolition measurements despite the absence of shielding elements. This compatibility between superconducting circuits and telecom wavelength light is not only a prerequisite to establish modular quantum networks [11], it is also relevant for multiplexed readout of superconducting photon detectors [12] and classical superconducting logic [13]. Moreover, this experiment showcases the potential of electro-optic radiometry in harsh environments - an electronics-free sensing principle that extends into the THz regime with applications in radio astronomy, planetary missions and earth observation [14].

The increasing demand for higher data transfer rates and energy efficiency alike has set the path to replacing electrical components by their optical counterparts. This is because of the substantially larger bandwidth of optical signals and the exceptionally low transmission loss in fibers at telecom wavelengths. Recently, this transition affects not only long-distance communication but also short-range links within data centers [3] or even on a single chip [15]. Moving the processors into a cryogenic environment can decrease the power consumption of computation even further [16], increase the sensitivity of detection systems [12], and interface classical control systems with cryogenic quantum processors directly [17]. However, such an approach is also susceptible to transmission losses and related heating in electrical wires and thus might also benefit from a suitable, low-loss and low thermal conductivity optical [13] or contactless [18] links.

Quantum processors, such as superconducting platforms that operate at ultra-low temperatures of a few millikelvin, have particularly demanding I/O requirements. In stark contrast to classical processors, herein the number of external control and readout lines scales linearly with the number of qubits. Currently, the most powerful quantum processors utilize more than 100 qubits requiring hundreds of high-bandwidth coaxial cables with appropriate signal conditioning [19], i.e. attenuation and careful thermalization on the input as well as isolation and low noise amplification on the output, see Fig. 1a. Considering the limited cooling power of dilution refrigerators, this architecture might allow for thousands of

qubits [20] given that advanced multiplexing strategies are employed [21–23]. This is - ignoring space and financial constraints - still orders of magnitudes beneath the millions of qubits expected to be required for fault-tolerant universal quantum computing [1, 24, 25].

Searching for ways to overcome these barriers, photonic links [5–7] were identified as a promising alternative to conventional [20], cryo-CMOS [17] or single flux quantum control [26] of cryogenic quantum computing platforms. The first optical interconnect with a superconducting qubit detected the average optical power emitted from the qubit - a destructive measurement that prevented further use of the qubit state [9]. Low back-action qubit readout has also recently been shown with a mechanically mediated electro-optical interconnect [8] in a scheme comparable to Fig. 1b, but this relatively low bandwidth method necessitates additional microwave pumps with the associated heat load and isolation requirements. Ultra-high bandwidth readout of an electro-mechanical system has been demonstrated with a commercial electro-optic modulator operated at 4 K but with limited efficiency and noise performance [7]. On the input side, high-speed photodetectors have been used to demodulate microwave control and readout signals [6]. This is a promising approach for multiplexed control but necessarily dissipative and does not allow to convert the readout signals back to the optical domain.

In this paper, we demonstrate all-optical single-shot readout of a superconducting qubit, i.e. we replace both the input and output signal path by one optical fiber each, as shown in Fig. 1c. Using a single electro-optic interconnect, i.e. a triply resonant whispering gallery mode single-sideband transducer [27–30], we simultaneously modulate and demodulate the optical carrier at millikelvin temperatures. This allows for a novel circulator-

[†] georg.arnold@ist.ac.at

[‡] jfink@ist.ac.at

* These authors contributed equally to this work.

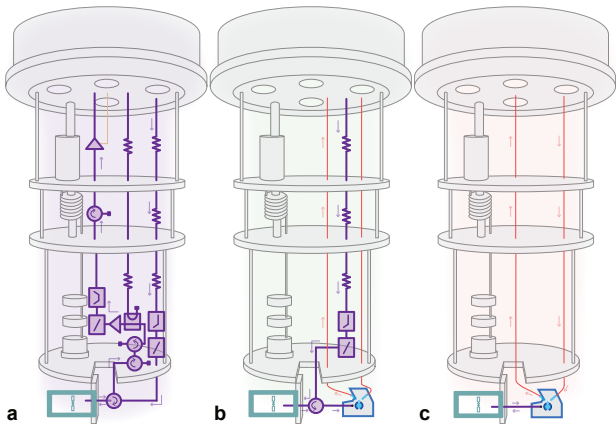


FIG. 1. **Comparison of conventional and optical qubit readout setups in a dilution refrigerator.** **a**, microwave in - microwave out: Typical setup consisting of carefully thermalized coaxial cables, attenuators, filters, circulators, a directional coupler, a driven parametric amplifier, and a de-biased high-electron-mobility-transistor amplifier, all of which are approximately wavelength sized (centimeters). **b**, microwave in - optics out: Reduced readout setup replacing the active microwave output components with an optically driven, resonant electro-optic transceiver. **c**, optics in - optics out: all-optical, circulator-free qubit readout based on simultaneous microwave down- and up-conversion of an optical carrier. Here, all cryogenic microwave components are replaced by a single electro-optic transceiver.

free readout that is used for time-domain characterization of a superconducting transmon qubit enclosed in a 3D superconducting cavity (cQED system) [31]. The latter is directly connected to the EO transceiver via a short coaxial cable without the need of any other cryogenic microwave components. The ability to perform both microwave and optical measurements allows to make a quantitative comparison of the assignment fidelity of different readout types. It also enables sensitive Josephson parametric amplifier measurements in the presence of the readout laser. We employ that to carefully quantify the potential radiation and average thermal impact on the mode occupancy and coherence of a superconducting processor that is operated with laser light.

Dynamics and single-shot fidelity of conventional and optical readout methods

We start with a comparison of the three different readout methods schematically depicted in Fig. 1 (see SI for detailed experimental setup): (i) *all-microwave readout* (Fig. 2a) with a microwave tone sent through coaxial cables to the cQED system and detected with a standard microwave heterodyne setup, (ii) *microwave-optic readout* with optical detection of the same microwave signal as in (i) from the cQED component after using it for the modulation of laser light via the EO transceiver (Fig. 2b), and (iii) *all-optical readout*: We send modulated light to the EO transceiver. The demodulated

microwave pulse enters the cQED system and its reflection is converted back into the optical domain using the same EO transceiver before being analyzed with an optical heterodyne detector at room temperature (Fig. 2c). All three schemes can be realized without setup changes except for the state of a cryogenic RF switch, as shown in Fig. 2a-c. While the first two methods can be performed simultaneously, opening the RF switch prevents the optically demodulated microwave signal in the all-optical readout from entering the microwave output line, which also effectively removes the circulator.

The operation frequency of the photonic link is determined by its optical free-spectral range $\omega_{\text{FSR}}/(2\pi) = 8.8065$ GHz set by the diameter of the lithium niobate resonator. To achieve a triply-resonant configuration that maximizes the transduction efficiency, we tune the electro-optic microwave cavity in resonance $\omega_e = \omega_{\text{FSR}}$ [27]. Similarly, to maximize the dispersive qubit readout efficiency [32] we also tune the cQED cavity to the same frequency $\omega_c = \omega_{\text{FSR}}$. Both are implemented with a piezoelectric actuator.

The transmon qubit with anharmonicity $\nu/(2\pi) = 201$ MHz is alternately prepared in its first excited state $|e\rangle$ or thermalized in its ground state $|g\rangle$ by selectively applying a flat-top-Gaussian microwave pulse of duration 104 ns at the qubit transition frequency $\omega_q/(2\pi) = 6.625$ GHz via a dedicated drive line, as shown in Fig. 2a-c. The readout tone, on the other hand, is either applied via filtered and attenuated input coaxial lines (Fig. 2a-b) or directly generated by the electro-optic transceiver (Fig. 2c) via resonantly enhanced optical down-conversion [33]. The readout amplitude corresponding to approximately $\sqrt{n_{\text{meas}}} = 122$ photons^{1/2} in the cavity is chosen to optimally benefit from the Jaynes-Cummings nonlinearity of the qubit-cavity system [34, 35] that maps the qubit-state-dependent dispersive frequency shift of the resonator $\chi/(2\pi) = 6.6$ MHz into a large readout amplitude difference at the bare cQED cavity frequency ω_e , see SI for details. The latter allows for single-shot readout of the qubit state without a quantum-limited amplifier [10].

Figure 2d shows the ensemble averaged reflection amplitude from heterodyne detection in power units for the all-microwave readout. The measured dynamics with the qubit initialized in its ground state is in excellent agreement with the input-output relations taking into account the reflection from the transducer microwave cavity (gray line, see SI) as part of the signal output path. When the qubit is prepared in the excited state, the nonlinear dynamics switches the cQED cavity reliably to its bare frequency for the same readout power, which effectively results in a critically coupled configuration and a vanishing reflection. While the dynamics are out of reach to be modeled given the high photon numbers, we adopt a simple cascaded cavity model between the cQED cavity and the EO microwave cavity [36]. This accurately predicts the steady-state result after times $> 1.0 \mu\text{s}$ without free parameters (black line highlighted with an arrow,

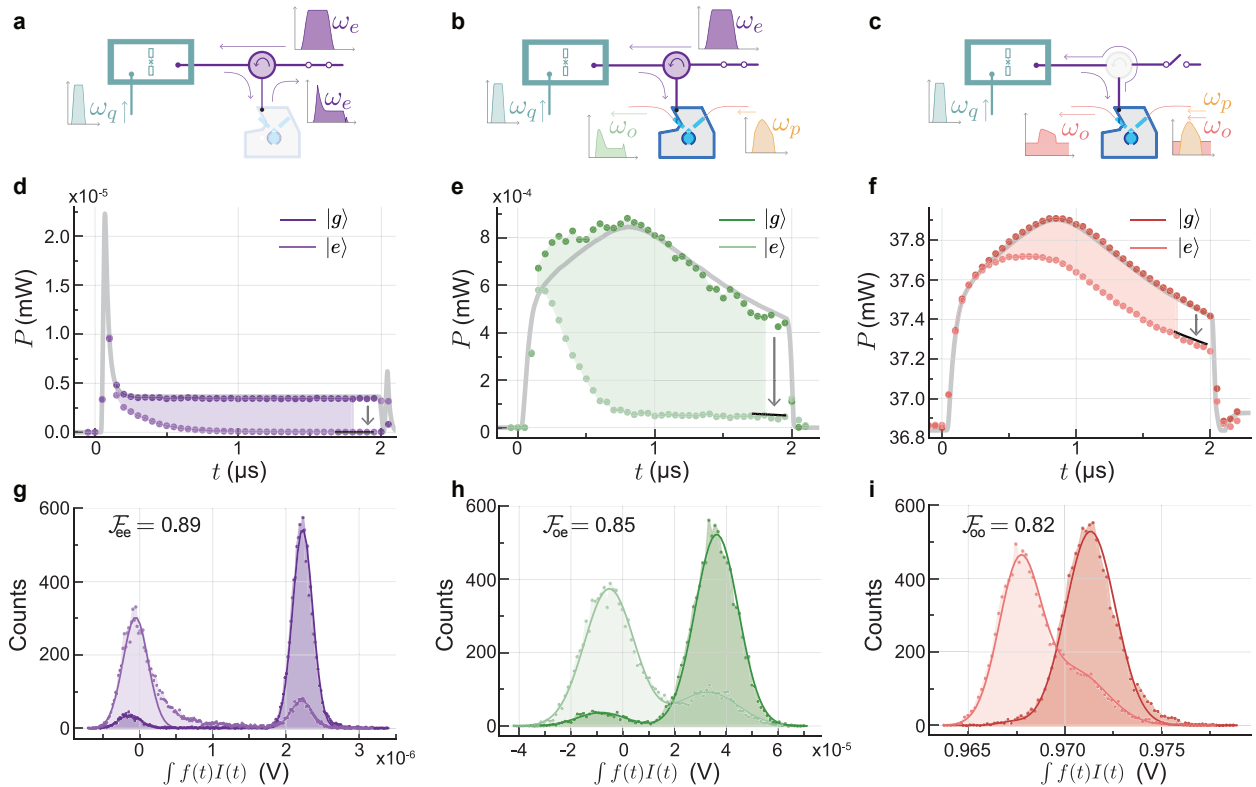


FIG. 2. **Conventional and optical single-shot readout of a superconducting qubit.** **a,b,c**, Sketches of the different readout schemes involving a microwave cavity dispersively coupled to a transmon qubit (cQED system in jade) and the electro-optical transceiver, consisting of a second microwave cavity (blue/gray) coupled to an optical whispering gallery mode resonator (light blue). The qubit state is prepared via a separate port at ω_q . The electro-optic transceiver is operated with an optical pump pulse at ω_p to parametrically enhance the interconversion of microwave ω_e and optical ω_o signals. **a**, Conventional microwave readout: a microwave pulse probes the cQED system and is detected via microwave heterodyne detection. **b**, Optical detection of a microwave readout tone: the microwave pulse reflected from the cQED system is upconverted to the optical domain and detected with optical heterodyne detection. **c**, All-optical readout: a modulated optical carrier is converted to the microwave domain to probe the cQED system. Its reflection is simultaneously converted back to the optical domain and detected with an optical heterodyne setup. **d, e, f**, Averaged time traces of the correspondingly measured heterodyne signal powers for the qubit prepared either in the $|g\rangle$ or $|e\rangle$ state based on 15,000 independent measurements. The shaded area highlights the difference between both qubit states, which serves as an appropriate weighting function $f(t)$ for the time trace integration. **g, h, i**, Corresponding histograms of 15,000 single-shots obtained by integrating the weighted in-phase quadrature $f(t)I(t)$ with the corresponding state assignment fidelities \mathcal{F}_{ij} .

cf. also SI) and consequently the readout contrast between both states. We then use these averaged measurements to find the optimal quadrature rotation and the integration weights (shaded region in Fig. 2d) that maximize the distinguishability for the single-shot-readout.

We show the corresponding single-shot histograms from 1.5×10^4 independent measurements for each qubit state in Fig. 2g with double-Gaussian fits [37]. The maximum state assignment fidelity of $\mathcal{F}_{ee} = 1 - (P(e|g) + P(g|e))/2 = 0.89 \pm 0.01$ is reached after an integration time of 1.8μ s, with $P(x|y)$ being the probability to measure the qubit in state $|x\rangle$ after preparation of state $|y\rangle$. The clear separation between the two distributions indicates a negligible overlap error ($\epsilon_{ol,e} < 10^{-10}$). The ground state error ($\epsilon_{g,e} \approx 7\%$) originates partly

from thermal excitation (1.5% as quantified below), while the rest is attributed to transitions induced by the comparably long high power readout pulse [38]. The excited state readout results in an error of $\epsilon_{e,e} \approx 16\%$, which suffers additionally from qubit decay during the measurement, shown as an asymmetric tail in the excited state Gaussian towards the ground state distribution.

For a direct comparison, we simultaneously also read out a small part of the reflected microwave readout tone optically, as shown in Fig. 2b. After resonantly enhanced microwave to optical conversion [33], in which about 3% of the intra-cavity microwave photons are converted, we perform optical heterodyne detection, which yields the averaged time traces shown in Fig. 2e. In comparison to the microwave readout, we find slower dynam-

ics and an additional decay of the optical readout signal at $\omega_o/(2\pi) = 193.4$ THz. This is due to the limited conversion bandwidth of ≈ 10 MHz and the particular shape of the ≈ 140 mW parametric optical pump pulse at frequency $\omega_p = \omega_o - \omega_{\text{FSR}}$ in very good agreement with theory (gray line) and the steady-state prediction (black line). As a result, the separation between the single-shot state distributions decreases (Fig. 2h), resulting in a larger overlap error of $\epsilon_{ol, eo} = 2\%$ and a slightly reduced microwave-optical state assignment fidelity of $\mathcal{F}_{oe} = 0.85 \pm 0.01$.

Finally, also in case of the all-optical readout the optically demodulated microwave tone (corresponding to $\sqrt{n_{\text{meas}}} = 116$ photons^{1/2} in the cQED cavity) results in well-distinguished state dependent trajectories as shown in Fig. 2f. The large optical background signal is due to the cumulative reflection of the optical input e.g. at the coupling prism. The bandwidth of the EO transceiver now also slows down the dynamics of the build-up of microwave readout photons. Taking also into account the effect of electro-optically induced transparency [39], which raises both signal levels during the optical pulse, the data is in excellent agreement with theory (gray and black lines). The moderate reduction of fidelity $\mathcal{F}_{oo} = 0.82 \pm 0.01$ can be fully attributed to the larger overlap error between the state distributions shown in Fig. 2i. This result proves the feasibility of an isolator-free qubit readout without cryogenic microwave components.

Time-dependent qubit measurements

We use all three readout methods to extract the longitudinal T_1 and transverse relaxation time T_2^* of the superconducting qubit, based on 2,000 preparations with a 10 Hz repetition rate. Figure 3a shows the energy relaxation after a π -pulse yielding a consistent T_1 of 31.1 to 35.4 μs for the three readout types. The observed differences are in line with expected T_1 variability over the course of days. The individual signal-to-noise ratio and resulting confidence level is very similar for all three measurements and the slightly reduced contrast is expected due to the previously extracted \mathcal{F}_{ij} .

Similar conclusions can be drawn from the measured exponential decay of the Ramsey oscillations shown in Fig. 3b. The fitted mean transverse decays for all three measurements, $T_2^* = 1.16 - 1.73$ μs , are comparable with the all-optical readout yielding the longest coherence. We attribute the comparably low T_2^* of this particular device to fabrication and design-related issues, as the theoretical limit due to energy decay and dephasing from thermal cavity shot noise [40] is estimated to be $T_2^* \approx 20.0$ μs and a Hahn-echo measurement of $T_{2, \text{echo}} = (1.40 \pm 0.03)$ μs excludes a low frequency, e.g. mechanical, noise origin. Moreover, we observe the same coherence times when the readout laser is turned off, or when the optical pulse is applied during the qubit state preparation, as discussed below. Our measurements, therefore, clearly demonstrate the integrity of superconducting qubit coherence using a

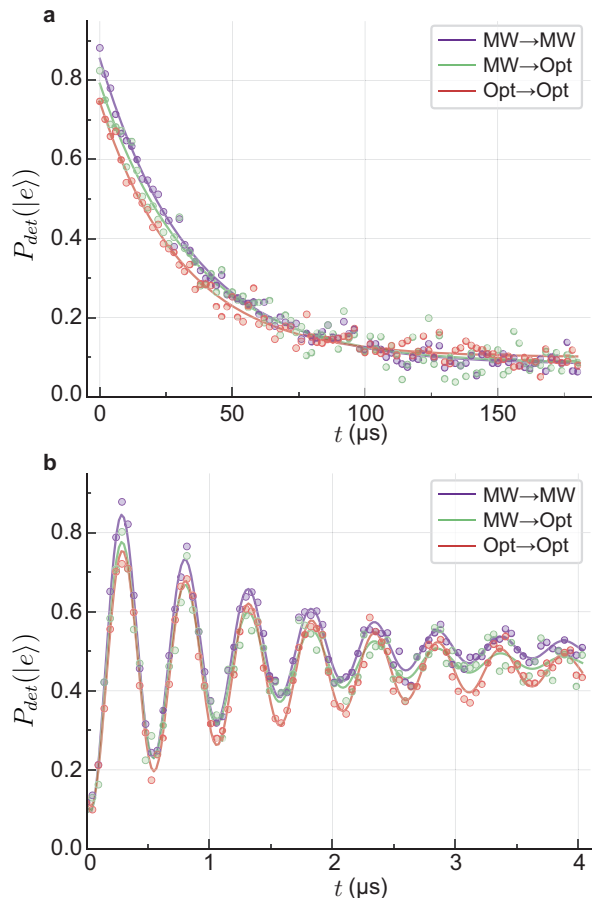


FIG. 3. **Qubit coherence for different readout methods.** **a**, Measured excited state detection probability $P_{\text{det}}(|e\rangle)$ after a π pulse for varying measurement delays t using the three different readout methods shown in Fig. 2. **b**, Measured Ramsey oscillations using two $\pi/2$ pulses separated by a variable delay t and detuned by ≈ 2 MHz from the qubit transition for the three readout methods.

photonic readout.

Impact of optical absorption heating quantified with quantum-non-demolition measurements

While the previous measurements have shown that reliable qubit characterization is feasible with a strong optical readout pulse, a more sensitive method is required to fully quantify the potential radiative [41, 42] and thermal [28] impact of high energy pump photons. In the following, we use a near-quantum-limited non-degenerate Josephson parametric amplifier [43] to perform a low power, dispersive, and non-destructive qubit readout to quantify such effects.

First, we measure the alternately prepared qubit states two times back to back, the first one in the presence of the previously used optical pump pulse and for comparison also when the laser is off. Figure 4a shows the extracted assignment fidelity \mathcal{F} of the first (second) mea-

surement in cyan (green) for increasing optical pulse repetition rates. The observed dependence on the resulting applied average optical power (top axis) is in excellent agreement with theory (lines and 3σ confidence bands) for spontaneous emission scaling with $1 - e^{-t/T_1}$ and the independently measured thermal excitation of the qubit, cf. Fig. 4c. The remaining discrepancy is fitted to be $\leq 1\%$ and attributed to either measurement (or optical radiation) induced transitions or state preparation errors.

The quantum-non-demolition (QND) metric is defined as the fraction of measurements, where two consecutive measurements yield the same qubit state [44], i.e. $Q = (P(g_2|g_1) + P(e_2|e_1))/2$. Importantly, Q (orange) is comparable for moderate repetition rates and a dark measurement without laser light, which implies a minimal (if any) direct impact of the optical pulse on the qubit. This interpretation is backed by additional measurements where the same optical pulse is applied during the qubit state preparation (open symbols in Fig. 4), which mostly overlap. The theoretical prediction is based on spontaneous emission.

Figure 4b shows the identically measured qubit coherence times as a function of optical pulse repetition rate (open circles) together with free-running measurements where the optical pulse is not synchronized with the microwave measurements (≈ 5 kHz repetition rate, solid circles). The latter method is faster but would not reveal an instantaneous radiation-based impact, e.g. via the generation of quasiparticles. The very close agreement between the two types of measurements (most symbols overlap), the small difference between low repetition rates and laser-off measurements, and the very good agreement with the coherence times obtained with the optical readout of Fig. 3 (black squares) indicates the absence of such radiative effects.

The measured reduction in T_1 as a function of applied average optical power is in excellent agreement with optical absorption heating in the EO transducer. The theory curve in Fig. 4b (red line and 3σ confidence band) takes into account thermal radiation [45] and thermal equilibrium quasiparticles with a superconducting gap of $\Delta = 205 \mu\text{eV}$ using the independently measured qubit temperature shown in Fig. 4c, as well as a typical nonequilibrium quasiparticle density of 1×10^{-7} [46], and an increase in the Purcell rate due to a somewhat broadened cQED cavity linewidth at higher repetition rates and temperatures. The relative dependence of the transverse decay T_2^* , however, cannot be explained by an increase in shotnoise dephasing from the thermally populated cQED cavity [40] (light blue line), similar to its absolute value (cf. discussion Fig. 3b). $T_{2,\text{echo}}$ and T_2^* show again no measurable difference. Quasiparticles are also not believed to have a dominating effect on dephasing in transmon qubits [47–49].

Finally, we investigate the average temperature distribution of the different components, which is used for the theory in Fig. 4a and b. Fig. 4c shows the measured base plate temperature from a calibrated ruthenium ox-

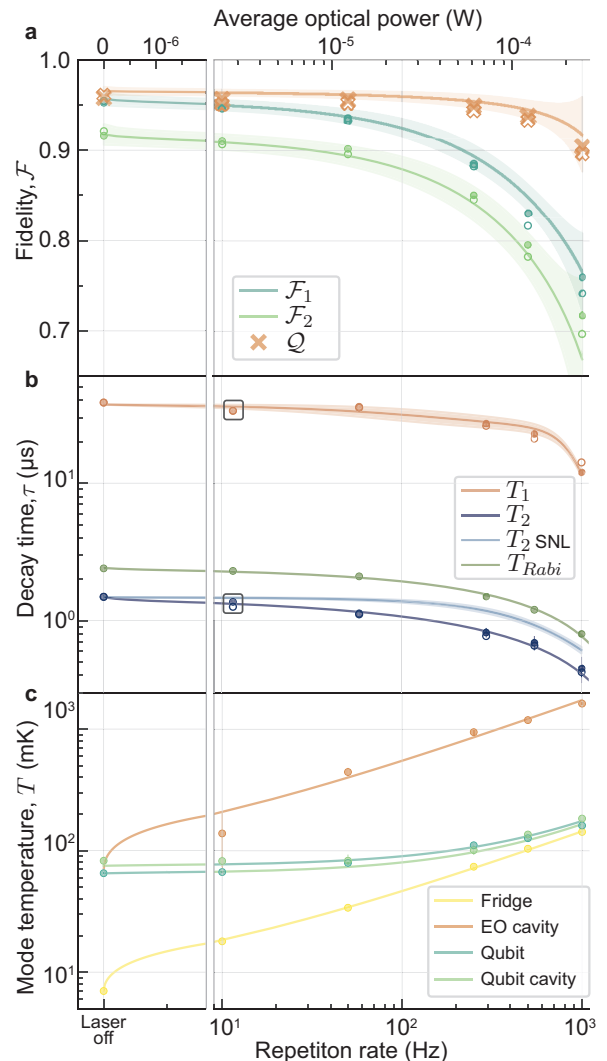


FIG. 4. **Impact of the optical pump.** **a**, Measured state assignment fidelities of two consecutive JPA-assisted microwave measurements (dots) and corresponding QND metric (crosses) obtained in the presence of a $2 \mu\text{s}$ long optical pump pulse of ≈ 0.14 W applied during the first readout as a function of repetition rate and calculated average optical power (top axis) together with theory (lines and 3σ confidence bands). Open symbols (mostly overlapping) denote measurements where the optical pump was applied during state preparation. **b**, Measured qubit coherence times when the optical pulse is synchronized with each state preparation and readout (open circles) and for a free-running measurement sequence (dots) vs. optical pulse repetition rate. Squares indicate the mean of the optical readout results in Fig. 3. The decrease in T_1 is accurately modelled with theory (red line and 3σ confidence band) but the shot noise dephasing limit (blue line) does not capture the measured T_2 dependence, which follows a $\propto -x^{0.37}$ power law (dark blue line) similar to the measured Rabi decay (green). **c**, Measured temperature of the mixing chamber (yellow dots) and the different microwave modes (dots) together with power law fits as a guide to the eye.

ide sensor, as well as the mode temperature of the superconducting qubit as obtained from thermally excited $|e\rangle \leftrightarrow |f\rangle$ Rabi oscillations [50]. The temperature of the cQED cavity is extracted from populated Ramsey oscillations [51], and the EO microwave cavity temperature is calculated from the measured power spectral density at its output [28]. These measurements were performed free-running but with the same optical pulse applied to the transducer.

When the laser is off, all components thermalize to a temperature of ≈ 75 mK, while the refrigerator reaches a base temperature of ≈ 7 mK, see Fig. 4c. When the optical pump is on, it acts as a localized heat source that increases the EO microwave mode temperature (orange). The proportionality to the time-averaged applied optical power of $\propto \bar{P}_{\text{opt}}^{0.54}$ agrees with previous findings for continuous wave optical pumps [28]. The EO transceiver is in very good thermal contact to the refrigerator's base plate, which heats up the refrigerator with the same power law (yellow). The resilience of the cQED system to radiation and heating at moderate repetition rates (cf. Fig. 4a and b) is reflected again in the mode temperature of the qubit and the dispersively coupled cavity. Their temperature increases only slightly compared to the laser-off situation for moderate repetition rates. One reason for this behavior is the detuning between the transducer cavity mode and the cQED system by the Lamb shift $\chi_0/(2\pi) = 26$ MHz except for the moment when the high power readout pulse is applied. Other reasons are the careful thermalization of all components and the large heat capacity and thermal contact area of the bulk EO transducer compared to integrated photonics approaches. However, as the cQED system is thermally connected to the mixing chamber as well, its mode temperature rises as soon as the fridge temperature approaches the thermalization temperature of the cQED unit (cyan and light green). This behavior is consistent with the sharp decline in the qubit coherence and readout fidelity for higher repetition rates in Fig. 4a and b.

Conclusions and prospects

One of the main motivation for this work is to simplify the cryogenic measurement setup by eliminating bulky and costly microwave components that are the source of a significant heat load [20]. In contrast, even the smallest cooling power at the mixing chamber plate can handle the passive heat load of millions of fibers [6] and their small cross-section mitigates the problem of space constraints raised by mm-sized coaxial cables. Nevertheless, the active heat load of this proof-of-principle all-optical readout limits the duty cycle and prevents a direct scaling-up to many readout-out lines. In the present case, due to our low optical coupling efficiency of $\eta_o = 0.22$, a majority of the parametric pump power is absorbed at the mixing chamber, leading to the observed temperature increase associated degradation of the qubit coherence shown in

Fig. 4. In the future, the optical coupling efficiency is therefore a critical parameter to improve, and optimized devices will also need to out-couple the majority of the reflected light to avoid absorption in the refrigerator. Similarly, the power efficiency is another critical parameter that can be improved dramatically with integrated photonic devices. One example is an electro-opto-mechanical device yielding a similar cooperativity for 10^{-9} times lower optical pump power [52] albeit with lower bandwidth and noise performance.

One of the limitations of the presented optical readout is the need for a comparably large number of readout photons n_{meas} . Scaling the histograms in Fig. 2g-i with the corresponding readout amplitude $\sqrt{n_{\text{meas}}}$ yields the quantum efficiency $\eta_{\text{det}} = \sigma_0^2/\sigma_{\text{det}}^2$ with the Gaussian variance of the measured histogram σ_{det}^2 and the variance of an ideal phase insensitive amplifier $\sigma_0^2 = 0.5$ [53]. For the conventional microwave readout (without JPA) we extract $\eta_{\text{det,mw}} \approx 1.3 \times 10^{-3}$. This is consistent with a comparably large amount of loss between the cQED system and the first amplifier (transmission of only $< 3\%$) due to the extra circuit elements such as the EO converter with reflectivity $(1 - 2\eta_e)^2 = 0.09$, with the microwave coupling efficiency η_e . For the two optical readouts on the other hand we find $\eta_{\text{det,opt}} \approx 1.5 \times 10^{-4}$, which agrees with the moderate total electro-optic device conversion efficiency $\eta_{eo} = 0.3\%$ and optical losses. This is in the same ballpark as recent experiments with an electro-opto-mechanical system using a longer ($15 \mu\text{s}$) readout pulse [8]. Importantly, even with just the original performance of this device [33] (we observed optical Q degradation in repeated cooldowns) a quantum-non-demolition single-shot readout without electronic amplifiers and readout times of $\approx 1 \mu\text{s}$ would be within reach. With further realistic improvements of in/out coupling and transmission losses close to quantum limited detection efficiencies for photonic RF sensing [14] as well as high bandwidth and high fidelity qubit readout comparable to the state of the art [37] will be possible.

In summary, we have demonstrated a circulator-free superconducting qubit readout with an all-optical scheme that relies only on optical (de-)modulation and optical heterodyne detection. Such a platform offers a significantly simplified cryogenic setup where signal-conditioning is performed at room temperature and optical fibers act as link to the cryogenic environment. Somewhat surprisingly we found that the comparably high power optical pulse in the 100 mW range does not have a detrimental effect on the qubit coherence, despite the absence of shielding elements. This result, when combined with recent integrated photonics demonstrations of more power-efficient and higher repetition rate optical control [54] and readout [55] of planar superconducting qubits, provides a viable path towards all-integrated photonic operation of superconducting quantum processors.

-
- [1] S. Bravyi, O. Dial, J. M. Gambetta, D. Gil, and Z. Nazario, *Journal of Applied Physics* **132**, 160902 (2022).
- [2] M. E. Beverland, P. Murali, M. Troyer, K. M. Svore, T. Hoeffler, V. Kliuchnikov, G. H. Low, M. Soeken, A. Sundaram, and A. Vashchillo, Assessing requirements to scale to practical quantum advantage (2022), [arXiv:2211.07629](https://arxiv.org/abs/2211.07629).
- [3] Q. Cheng, M. Bahadori, M. Glick, S. Rumley, and K. Bergman, *Optica* **5**, 1354 (2018).
- [4] X. Han, W. Fu, C.-L. Zou, L. Jiang, and H. X. Tang, *Optica* **8**, 1050 (2021).
- [5] S. Joshi and S. Moazeni, Scaling up superconducting quantum computers with cryogenic rf-photonics (2022), [arXiv:2210.15756](https://arxiv.org/abs/2210.15756).
- [6] F. Lecocq, F. Quinlan, K. Cicak, J. Aumentado, S. A. Diddams, and J. D. Teufel, *Nature* **591**, 575 (2021).
- [7] A. Youssefi, I. Shomroni, Y. J. Joshi, N. R. Bernier, A. Lukashchuk, P. Uhrich, L. Qiu, and T. J. Kippenberg, *Nature Electronics* **4**, 326 (2021).
- [8] R. D. Delaney, M. D. Urmey, S. Mittal, B. M. Brubaker, J. M. Kindem, P. S. Burns, C. A. Regal, and K. W. Lehnert, *Nature* **606**, 489 (2022).
- [9] M. Mirhosseini, A. Sipahigil, M. Kalaei, and O. Painter, *Nature* **588**, 599 (2020).
- [10] M. D. Reed, L. DiCarlo, B. R. Johnson, L. Sun, D. I. Schuster, L. Frunzio, and R. J. Schoelkopf, *Phys. Rev. Lett.* **105**, 173601 (2010).
- [11] J. Ang, G. Carini, Y. Chen, I. Chuang, M. A. DeMarco, S. E. Economou, A. Eickbusch, A. Faraon, K.-M. Fu, S. M. Girvin, M. Hatridge, A. Houck, P. Hilaire, K. Krulich, A. Li, C. Liu, Y. Liu, M. Martonosi, D. C. McKay, J. Misewich, M. Ritter, R. J. Schoelkopf, S. A. Stein, S. Sussman, H. X. Tang, W. Tang, T. Tomesh, N. M. Tubman, C. Wang, A. N. Wiebe, Y.-X. Yao, D. C. Yost, and Y. Zhou, Architectures for Multinode Superconducting Quantum Computers (2022), [arXiv:2212.06167](https://arxiv.org/abs/2212.06167).
- [12] M. de Cea, E. E. Wollman, A. H. Atabaki, D. J. Gray, M. D. Shaw, and R. J. Ram, *Scientific Reports* **10**, 9470 (2020).
- [13] M. Shen, J. Xie, Y. Xu, S. Wang, R. Cheng, W. Fu, Y. Zhou, and H. X. Tang, Photonic link from single flux quantum circuits to room temperature (2023), [arXiv:2309.03284](https://arxiv.org/abs/2309.03284).
- [14] G. S. Botello, F. Sedlmeir, A. Rueda, K. A. Abdalmalak, E. R. Brown, G. Leuchs, S. Preu, D. Segovia-Vargas, D. V. Strekalov, L. E. G. M. noz, and H. G. L. Schwefel, *Optica* **5**, 1210 (2018).
- [15] C. Sun, M. T. Wade, Y. Lee, J. S. Orcutt, L. Alloatti, M. S. Georgas, A. S. Waterman, J. M. Shainline, R. R. Avizienis, S. Lin, B. R. Moss, R. Kumar, F. Pavanello, A. H. Atabaki, H. M. Cook, A. J. Ou, J. C. Leu, Y. H. Chen, K. Asanović, R. J. Ram, M. A. Popović, and V. M. Stojanović, *Nature* **528**, 534 (2015).
- [16] D. S. Holmes, A. L. Ripple, and M. A. Manheimer, *IEEE Transactions on Applied Superconductivity* **23**, 1701610 (2013).
- [17] S. J. Pauka, K. Das, R. Kalra, A. Moini, Y. Yang, M. Trainer, A. Bousquet, C. Cantaloube, N. Dick, G. C. Gardner, M. J. Manfra, and D. J. Reilly, *Nature Electronics* **4**, 64 (2021).
- [18] J. Wang, M. I. Ibrahim, I. B. Harris, N. M. Monroe, M. I. Wasiq Khan, X. Yi, D. R. Englund, and R. Han, in *2023 IEEE International Solid-State Circuits Conference (ISSCC)* (2023) pp. 504–506.
- [19] Y. Kim, A. Eddins, S. Anand, K. X. Wei, E. van den Berg, S. Rosenblatt, H. Nayfeh, Y. Wu, M. Zaletel, K. Temme, and A. Kandala, *Nature* **618**, 500 (2023).
- [20] S. Krinner, S. Storz, P. Kurpiers, P. Magnard, J. Heinsoo, R. Keller, J. Lütolf, C. Eichler, and A. Wallraff, *EPJ Quantum Technology* **6**, 2 (2019).
- [21] Y. Chen, D. Sank, P. O’Malley, T. White, R. Barends, B. Chiaro, J. Kelly, E. Lucero, M. Mariantoni, A. Megrant, C. Neill, A. Vainsencher, J. Wenner, Y. Yin, A. N. Cleland, and J. M. Martinis, *Applied Physics Letters* **101**, 182601 (2012).
- [22] J. Heinsoo, C. K. Andersen, A. Remm, S. Krinner, T. Walter, Y. Salathé, S. Gasparinetti, J.-C. Besse, A. Potočnik, A. Wallraff, and C. Eichler, *Phys. Rev. Appl.* **10**, 034040 (2018).
- [23] R. Acharya, S. Brebels, A. Grill, J. Verjauw, T. Ivanov, D. P. Lozano, D. Wan, J. Van Damme, A. M. Vadiraj, M. Mongillo, B. Govoreanu, J. Craninckx, I. P. Radu, K. De Greve, G. Gielen, F. Catthoor, and A. Potočnik, *Nature Electronics* (2023).
- [24] C. Gidney and M. Ekerå, *Quantum* **5**, 433 (2021).
- [25] T. Hoeffler, T. Häner, and M. Troyer, *Commun. ACM* **66**, 82–87 (2023).
- [26] C. Liu, A. Ballard, D. Olaya, D. Schmidt, J. Biesecker, T. Lucas, J. Ullom, S. Patel, O. Rafferty, A. Opremcak, K. Dodge, V. Iaiia, T. McBroom, J. DuBois, P. Hopkins, S. Benz, B. Plourde, and R. McDermott, *PRX Quantum* **4**, 030310 (2023).
- [27] A. Rueda, F. Sedlmeir, M. C. Collodo, U. Vogl, B. Stiller, G. Schunk, D. V. Strekalov, C. Marquardt, J. M. Fink, O. Painter, G. Leuchs, and H. G. L. Schwefel, *Optica* **3**, 597 (2016).
- [28] W. Hease, A. Rueda, R. Sahu, M. Wulf, G. Arnold, H. G. Schwefel, and J. M. Fink, *PRX Quantum* **1**, 020315 (2020).
- [29] L. Fan, C.-L. Zou, R. Cheng, X. Guo, X. Han, Z. Gong, S. Wang, and H. X. Tang, *Science Advances* **4**, eaar4994 (2018).
- [30] R. Sahu, L. Qiu, W. Hease, G. Arnold, Y. Minoguchi, P. Rabl, and J. M. Fink, *Science* **380**, 718 (2023).
- [31] H. Paik, D. I. Schuster, L. S. Bishop, G. Kirchmair, G. Catelani, A. P. Sears, B. R. Johnson, M. J. Reagor, L. Frunzio, L. I. Glazman, S. M. Girvin, M. H. Devoret, and R. J. Schoelkopf, *Phys. Rev. Lett.* **107**, 240501 (2011).
- [32] A. Wallraff, D. I. Schuster, A. Blais, L. Frunzio, J. Majer, M. H. Devoret, S. M. Girvin, and R. J. Schoelkopf, *Phys. Rev. Lett.* **95**, 060501 (2005).
- [33] R. Sahu, W. Hease, A. Rueda, G. Arnold, L. Qiu, and J. M. Fink, *Nature Communications* **13**, 1276 (2022).
- [34] L. S. Bishop, E. Ginossar, and S. M. Girvin, *Physical Review Letters* **105**, 100505 (2010).
- [35] M. Boissonneault, J. M. Gambetta, and A. Blais, *Physical Review Letters* **105**, 100504 (2010).
- [36] C. W. Gardiner, *Physical Review Letters* **70**, 2269 (1993).
- [37] T. Walter, P. Kurpiers, S. Gasparinetti, P. Mag-

- nard, A. Potočník, Y. Salathé, M. Pechal, M. Mondal, M. Oppliger, C. Eichler, and A. Wallraff, *Phys. Rev. Appl.* **7**, 054020 (2017).
- [38] D. Sank, Z. Chen, M. Khezri, J. Kelly, R. Barends, B. Campbell, Y. Chen, B. Chiaro, A. Dunsworth, A. Fowler, E. Jeffrey, E. Lucero, A. Megrant, J. Mutus, M. Neeley, C. Neill, P. J. O’Malley, C. Quintana, P. Roushan, A. Vainsencher, T. White, J. Wenner, A. N. Korotkov, and J. M. Martinis, *Physical Review Letters* **117**, 190503 (2016).
- [39] L. Qiu, R. Sahu, W. Hease, G. Arnold, and J. M. Fink, *Nature Communications* **14**, 3784 (2023).
- [40] A. A. Clerk and D. W. Utami, *Physical Review A* **75**, 042302 (2007).
- [41] R. Barends, J. Wenner, M. Lenander, Y. Chen, R. C. Bialczak, J. Kelly, E. Lucero, P. O’Malley, M. Mariantoni, D. Sank, H. Wang, T. C. White, Y. Yin, J. Zhao, A. N. Cleland, J. M. Martinis, and J. J. Baselmans, *Applied Physics Letters* **99**, 2009 (2011).
- [42] M. Houzet, K. Serniak, G. Catelani, M. H. Devoret, and L. I. Glazman, *Physical Review Letters* **123**, 107704 (2019).
- [43] P. Winkel, I. Takmakov, D. Rieger, L. Planat, W. Hasch-Guichard, L. Grünhaupt, N. Maleeva, F. Foroughi, F. Henriques, K. Borisov, J. Ferrero, A. V. Ustinov, W. Wernsdorfer, N. Roch, and I. M. Pop, *Physical Review Applied* **13**, 24015 (2020).
- [44] S. Touzard, A. Kou, N. E. Frattini, V. V. Sivak, S. Puri, A. Grimm, L. Frunzio, S. Shankar, and M. H. Devoret, *Phys. Rev. Lett.* **122**, 080502 (2019).
- [45] A. D. Córcoles, J. M. Chow, J. M. Gambetta, C. Rigetti, J. R. Rozen, G. A. Keefe, M. B. Rothwell, M. B. Ketchen, and M. Steffen, *Appl. Phys. Lett.* **99**, 181906 (2011).
- [46] K. Serniak, M. Hays, G. De Lange, S. Diamond, S. Shankar, L. D. Burkhardt, L. Frunzio, M. Houzet, and M. H. Devoret, *Physical Review Letters* **121**, 157701 (2018).
- [47] G. Catelani, S. E. Nigg, S. M. Girvin, R. J. Schoelkopf, and L. I. Glazman, *Physical Review B* **86**, 184514 (2012).
- [48] S. Zanker and M. Marthaler, *Physical Review B* **91**, 174504 (2015).
- [49] D. Ristè, C. C. Bultink, M. J. Tiggelman, R. N. Schouten, K. W. Lehnert, and L. Dicarlo, *Nature Communications* **4**, 1 (2013).
- [50] X. Y. Jin, A. Kamal, A. P. Sears, T. Gudmundsen, D. Hover, J. Miloshi, R. Slattery, F. Yan, J. Yoder, T. P. Orlando, S. Gustavsson, and W. D. Oliver, *Physical Review Letters* **114**, 240501 (2015).
- [51] R. Dassonneville, R. Assouly, T. Peronnin, A. A. Clerk, A. Bienfait, and B. Huard, *PRX Quantum* **2**, 20323 (2021).
- [52] G. Arnold, M. Wulf, S. Barzanjeh, E. S. Redchenko, A. Rueda, W. J. Hease, F. Hassani, and J. M. Fink, *Nature Communications* **11**, 4460 (2020).
- [53] M. Hatridge, S. Shankar, M. Mirrahimi, F. Schackert, K. Geerlings, T. Brecht, K. M. Sliwa, B. Abdo, L. Frunzio, S. M. Girvin, R. J. Schoelkopf, and M. H. Devoret, *Science* **339**, 178 (2013).
- [54] Warner et al, K. H. and Holzgrafe, J. and Yankelevich, B. and Barton, D. and Poletto, S. and Xin, C. J. and Sinclair, N. and Zhu, D. and Sete, E. and Langley, B. Batson, E. and Colangelo, M. and Shams-Ansari, A. and Joe, G. and Berggren, K. K. and Jiang, L. and Reagor, M. and Lončar, M., Previous correspondence (2023).
- [55] T. C. van Thiel, M. J. Weaver, F. Berto, P. Duivestein, M. Lemang, K. Schuurman, M. Žemlička, F. Hijazi, A. C. Bernasconi, E. Lachman, M. Field, Y. Mohan, F. de Vries, N. Bultink, J. van Oven, J. Y. Mutus, R. Stockill, and S. Gröblacher, *High-fidelity optical readout of a superconducting qubit using a scalable piezo-optomechanical transducer* (2023), arXiv:2310.06026.

Data and Code Availability

The code and raw data used to produce the plots in this paper will be made available at the Zenodo open-access repository at the time of publication.

Acknowledgments

We thank F. Hassani and M. Zemlicka for assistance with qubit design and high power readout respectively, and P. Winkel and I. Pop at KIT for providing the JPA. This work was supported by the European Research Council under grant agreement no. 758053 (ERC StG QUNNECT) and no. 101089099 (ERC CoG cQEO), the European Union’s Horizon 2020 research and innovation program under grant agreement no. 899354 (FETopen SuperQuLAN) and the Austrian Science Fund (FWF) through BeyondC (grant no. F7105). L.Q. acknowledges generous support from the ISTFELLOW programme and G.A. is the recipient of a DOC fellowship of the Austrian Academy of Sciences at IST Austria.

Author Contributions

G.A. and T.W. performed the experiments together with R.S. and L.Q. G.A., R.S. and L.Q. developed the theory. G.A. and T.W. performed the data analysis. G.A. designed the qubit and developed the tunable microwave cavity, and L.K. fabricated the transmon qubit. The manuscript was written by G.A. and J.M.F. with assistance from all authors. J.M.F. supervised the project.

Competing Interests

The authors declare no competing interests.

Supplementary information ”All-optical single-shot readout of a superconducting qubit”

Georg Arnold^{*,1,*} Thomas Werner^{*,1} Rishabh Sahu,¹ Lucky N. Kapoor,¹ Liu Qiu,¹ and Johannes M. Fink^{1,†}

¹*Institute of Science and Technology Austria, Am Campus 1, 3400 Klosterneuburg, Austria*

(Dated: October 26, 2023)

CONTENTS

| | Page |
|--|------|
| I. Jaynes-Cumming nonlinearity readout and toy model | 3 |
| A Experimental observation | 3 |
| B Microwave readout model | 4 |
| C Microwave-optical readout model | 4 |
| D Full optical readout model | 4 |
| II. Fabrication | 5 |
| A The cQED system | 5 |
| B The electro-optic transceiver | 5 |
| III. Experiment | 5 |
| References | 7 |

arXiv:2310.16817v1 [quant-ph] 25 Oct 2023

* georg.arnold@ist.ac.at

† jfink@ist.ac.at

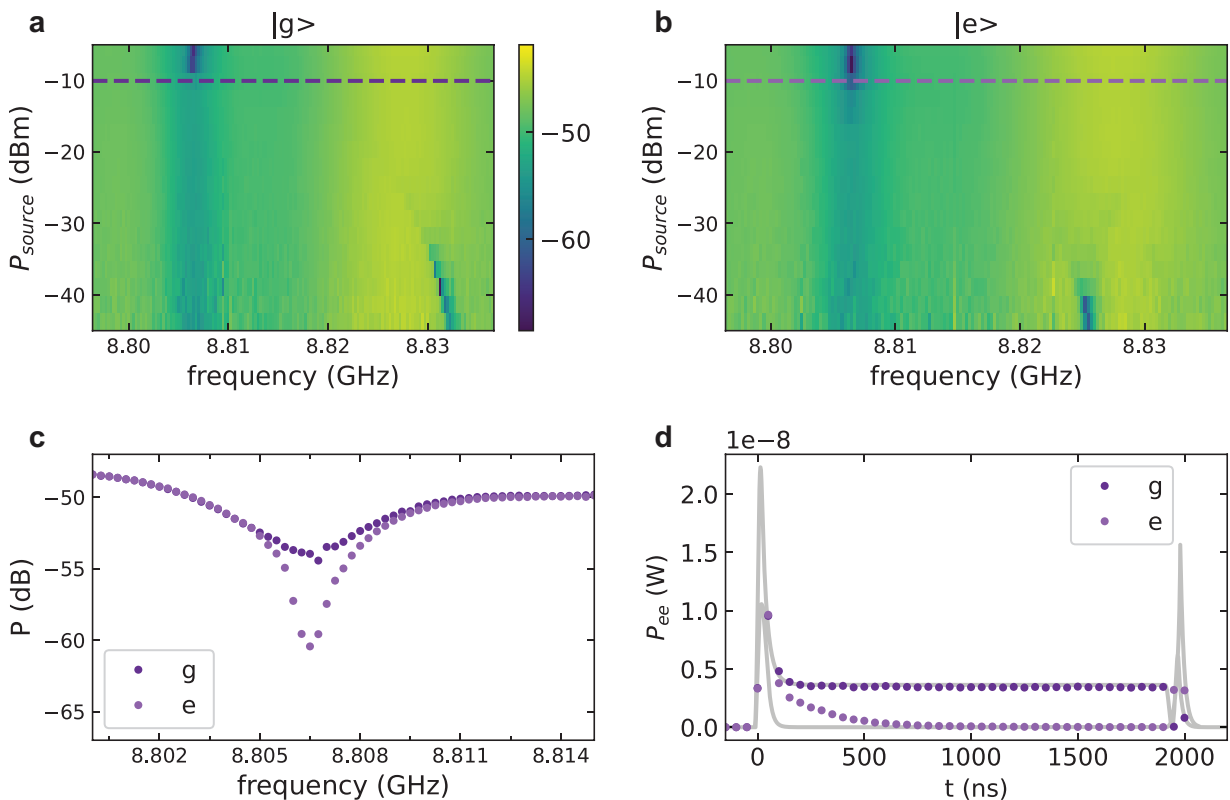
| Introduced in Main Text | |
|--|---|
| C | cooperativity ($C = 4g^2/\kappa_e\kappa_o$) |
| $\chi_{g,e}$ | Dispersive qubit-state-dependent frequency shift |
| χ_0 | Lamb shift |
| Δ | Superconducting gap |
| $\epsilon_{g,e}, \epsilon_{e,e}$ | Ground state, excited state error |
| $\epsilon_{ol,e}, \epsilon_{ol,oe}$ | Overlap error for mw, mw \rightarrow opt readout |
| $\eta_{det}, \eta_{det,mw}, \eta_{det,opt}$ | Quantum efficiency for microwave, optical detection |
| η_e | External coupling efficiency transducer cavity |
| η_{eo} | Total electro-optic conversion efficiency |
| $\sqrt{n_{meas}} / n_{meas}$ | Readout amplitude / readout photon number |
| η_o | External coupling efficiency optical resonator |
| $f(t)$ | Weighting function for time-trace integration |
| $\mathcal{F}_{ee}, \mathcal{F}_{oe}, \mathcal{F}_{oo}$ | Assignment fidelity for mw \rightarrow mw, mw \rightarrow opt, and opt \rightarrow opt readout |
| $ g\rangle, e\rangle, f\rangle$ | Qubit ground, excited, second excited state |
| $I(t)$ | In-phase quadrature of the microwave output field |
| mw \rightarrow mw, mw \rightarrow opt, opt \rightarrow opt | Sending and measuring microwaves, sending microwaves and measuring optics, sending and measuring optics |
| ν | Qubit level anharmonicity |
| ω_c | Resonance frequency of the cQED system |
| ω_{FSR} | Optical free spectral range |
| ω_e | Microwave resonance frequency of the electro-optic transducer |
| ω_o | Optical signal frequency |
| ω_p | Optical pump frequency |
| ω_q | First qubit transition frequency |
| $P(e g) (P(g e))$ | Probability for assigning $ e\rangle(g\rangle)$, after preparing $ g\rangle(e\rangle)$ |
| $P(e_1 e_2) (P(g_1 g_2))$ | Probability to measure $ e\rangle(g\rangle)$ in two successive measurements |
| P_{opt} | Optical power |
| \mathcal{Q} | Quantum non-demolition metric (QND-ness) |
| σ_{det}^2 | Scaled Gaussian variance |
| σ_0^2 | Variance ideal amplifier |
| T | Mode temperature |
| T_1 | Energy relaxation |
| $T_{2,echo}$ | Transverse echo relaxation |
| T_2^* | Transverse decay |
| Introduced in Supplementary information | |
| \hat{a}_j | Mode, $j \in (e, o, c, p, s, tm)$ |
| $\hat{a}_{j,in}$ | Input field (noise) operator for the microwave and optical mode, $j \in (e, o, c)$ |
| $\hat{a}_{j,out}$ | Readout field, $j \in (e, o, c)$ |
| δ_j | Detuning, $j \in (o, s, tm)$ |
| η_j | External cavity coupling efficiency of individual mode, $j \in (e, o, c, p)$ |
| $\eta_{j,i}$ | Coupling efficiency from i to j, $i, j \in (e, o, c)$ |
| f_{bare}, ω_{bare} | Bare resonator frequency cQED, $2\pi f_{bare}$ |
| g | Photon enhanced electro-optical coupling rate ($g = \bar{a}_p g_0$) |
| g_0 | Electro-optic vacuum coupling rate ($g = \bar{a}_p g_0$) |
| J | Coupling rate between the optical Stokes mode and TM mode |
| κ_j | Total loss rate of individual mode, $j \in (e, o, c, s, p)$ |
| $\kappa_{j,ex}$ | External loss rate of individual mode, $j \in (e, o, c)$ |
| m | Microwave azimuthal mode number, $m = 1$ |
| P_{ee} | Detected power for mw \rightarrow mw |
| $\hat{\sigma}_z$ | Pauli operator |
| τ | Delay |

Supplementary Tab. 1. List of variables.

I. JAYNES-CUMMING NONLINEARITY READOUT AND TOY MODEL

A. Experimental observation

In the dispersive limit, the nonlinearity from the Jaynes-Cumming interaction can be employed for a measurement of the qubit state with high signal-to-noise ratio [1]. The measurement effectively makes use of the qubit-induced cavity anharmonicity (Lamb shift $\chi_0/2\pi = 26$ MHz) which depends on the cavity drive power for higher occupations and the dispersive shift of the cavity at low drive powers ($\chi/2\pi = 6.6$ MHz). The combination of both effects leads to the shift of the cavity resonance to its bare frequency $f_{bare} = 8.806$ GHz at different drive powers for different qubit states. This allows a qubit state-dependent readout with high SNR (cf. dashed lines in Fig. 1a and b). Theoretical descriptions of this behavior include either higher qubit levels [2] or a semi-classical treatment for large cavity-qubit detunings and drive power-dependent anharmonicities [3]. Both models led to qualitative agreement of the frequency spectrum with the experimental observation. Phenomenologically, the situation can be described by the cQED cavity resonance either being at its bare resonator frequency ($|e\rangle$) or being completely off-resonant ($|g\rangle$). In our scheme, the microwave cavity of the electro-optic transducer is tuned to f_{bare} . Thus, one observes either the transducer cavity alone or on resonance with the cQED cavity by means of cascaded cavities (Fig.1c). Even though this omits the qubit-cavity interaction and can therefore not predict the temporal dynamics with the qubit being in $|e\rangle$, it is sufficient to model the system with independently calibrated parameters in steady state (Fig.1d).



Supplementary Fig. 1. **Jaynes-Cumming readout.** **a**, Microwave reflection spectrum from power sweep of the cascaded cQED-EO cavities with the qubit in ground state, the electro-optic transducer cavity at $\omega_e/2\pi = 8.806$ GHz, and additionally the cQED cavity switched to $\omega_{bare} = \omega_e$ at high readout powers. **b**, Similar spectrum to **a** with the qubit prepared in the excited state. The increased contrast due to the cQED cavity being resonant with the transducer cavity happens at slightly lower powers than for the ground state. **c**, Reflection for both qubit states at the microwave readout power used in the main text for the Jaynes-Cumming readout. The contrast difference allows to detect the qubit states at high powers at the bare cQED cavity frequency. **d**, Averaged time trace for the all-optical readout, presented in Fig.2d. Unlike in the main text, we additionally show the modelled time trace for the qubit in the excited state with our cascaded cavity toy model without a qubit. While the ground state response and the steady state of the excited state reached after $\approx 1 \mu\text{s}$ can be sufficiently described, the dynamics of the qubit-cavity interaction at smaller times naturally deviates.

B. Microwave readout model

We model the microwave system consisting of the cQED cavity and the transducer microwave cavity as two cascaded cavities with reflective ports (coupling $\eta\kappa$) and intrinsic loss rates $(1-\eta)\kappa$. Specifically, the microwave readout field from the cQED cavity $\hat{a}_{c,\text{out}}(t)$ travels through superconducting cables of efficiency $\eta_{e,c}$ and delay τ , and enters the microwave cavity of the electro-optical transducer with $\hat{a}_{e,\text{in}}(t) = \eta_{e,c}\hat{a}_{c,\text{out}}(t+\tau)$ [4].

If we send the specific readout power to the cQED device, at which the Jaynes-Cummings nonlinearity allows to detect the qubit state (Fig. 1c), the cQED cavity is either on-resonant with the transducer cavity ($\omega_e = \omega_c$, excited state) or completely reflective (ground state). We model the latter by a detuning χ_0 .

$$\dot{\hat{a}}_e = -\frac{\kappa_e}{2}\hat{a}_e + \sqrt{\eta_e\kappa_e}\eta_{e,c}\hat{a}_{c,\text{out}}, \quad (1)$$

$$\dot{\hat{a}}_c = \left[-i\frac{\chi_0}{2}(\langle\sigma_z\rangle + 1) - \frac{\kappa_c}{2}\right]\hat{a}_c + \sqrt{\eta_c\kappa_c}\hat{a}_{c,\text{in}}. \quad (2)$$

We model the system using decoupled equations assuming the signal propagation is unidirectional. This is a reasonable assumption because of the microwave circulator between both cavities. We want to stress again that this is only a phenomenological model to describe the behavior of the system at the specific power chosen for the Jaynes-Cummings readout.

C. Microwave-optical readout model

The microwave-optical readout of the qubit state is enabled by converting the microwave field from the cQED system into the optical domain using the electro-optic transducer. This allows for efficient conversion from microwave to optical fields. The electro-optic device is driven by a resonant optical pump pulse, with dynamics given by,

$$\dot{\bar{a}}_p = \left(i\Delta_p - \frac{\kappa_p}{2}\right)\bar{a}_p + \sqrt{\eta_p\kappa_p}\bar{a}_{p,\text{in}}, \quad (3)$$

with $g(t) = \bar{a}_p(t)g_0$ the cavity enhanced electro-optical coupling rate. The dynamics of the multi-mode electro-optic device can be described by the quantum Langevin equation,

$$\dot{\hat{a}}_e = -\frac{\kappa_e}{2}\hat{a}_e - ig\hat{a}_o - ig^*\hat{a}_s^\dagger + \sqrt{\eta_e\kappa_e}\hat{a}_{e,\text{in}}, \quad (4)$$

$$\dot{\hat{a}}_o = \left(i\delta_o - \frac{\kappa_o}{2}\right)\hat{a}_o - ig\hat{a}_e, \quad (5)$$

$$\dot{\hat{a}}_s = \left(i\delta_s - \frac{\kappa_s}{2}\right)\hat{a}_s - ig^*\hat{a}_e^\dagger - iJ\hat{a}_{\text{tm}}, \quad (6)$$

$$\dot{\hat{a}}_{\text{tm}} = \left(i\delta_{\text{tm}} - \frac{\kappa_{\text{tm}}}{2}\right)\hat{a}_{\text{tm}} - iJ\hat{a}_s. \quad (7)$$

where $a_{e,\text{in}}$ denotes again the output field from the cQED cavity. We note that, $J \ll \kappa_s$ in our device. The qubit state is verified by the converted optical Stokes output field from the electro-optic device,

$$\hat{a}_{o,\text{out}}(t) = -\sqrt{\kappa_{o,\text{ex}}}\hat{a}_o(t). \quad (8)$$

D. Full optical readout model

The full optical readout of the superconducting qubit is realized by sending an optical signal together with an optical pulse to the electro-optic transducer. The converted microwave signal is used for qubit readout and reflected back to the electro-optic transducer. The reflected microwave field is subsequently converted again into the optical domain. The dynamics of the electro-optic device from Eq. 4-7 is now related to the cQED system by

$$\hat{a}_{e,\text{in}}(t) = \eta_{e,c}\hat{a}_{c,\text{out}}(t), \quad (9)$$

$$\hat{a}_{c,\text{in}}(t) = \eta_{c,e}\hat{a}_{e,\text{out}}(t). \quad (10)$$

The superconducting qubit state thus can be verified from the reflected optical anti-Stokes field,

$$\hat{a}_{o,\text{out}}(t) = \hat{a}_{o,\text{in}}(t) - \sqrt{\kappa_{o,\text{ex}}}\hat{a}_o(t). \quad (11)$$

II. FABRICATION

A. The cQED system

For the fabrication of the transmon qubit, a $10 \times 10 \text{ mm}^2$ high resistivity silicon chip was cleaned using an O_2 plasma asher followed by a buffered oxide etch (BOE) dip for 30s. The chip is further cleaned by sonicating in 50°C acetone for 10 mins and finally rinsed with isopropyl alcohol (IPA). The cleaned chip is covered with double layer of MMA/PMMA resist to pattern the qubit with two capacitor pads of area $330 \times 550 \mu\text{m}^2$ separated by a $400 \mu\text{m}$ distance along with a Josephson junction in the center of the gap between the two capacitors. The entire process is performed in a single e-beam lithography (EBL) step using the Dolan bridge process for an $\text{Al}/\text{AlO}_x/\text{Al}$ junction of area $200 \times 300 \text{ nm}^2$. For the metal deposition, an in-situ gentle argon ion milling is performed to clean any resist residues from the surface of the silicon. The Josephson junction is then fabricated by evaporating 60 nm aluminum followed by static oxidation in pure O_2 environment and then a 120 nm thickness aluminum layer is evaporated. The residual metal is lifted off using dimethyl sulfoxide (DMSO) at 80°C for 3 hours followed by an acetone and IPA rinse. Finally, the sample is covered with S1805 photo resist and UV tape as the $10 \times 10 \text{ mm}^2$ chip is diced into three $10 \times 2.5 \text{ mm}^2$ pieces with one qubit on each diced chip.

The transmon qubit is strongly coupled to a $23 \times 15 \text{ mm}$ rectangular waveguide cavity with rounded sidewalls made of 6061 Aluminum alloy. Indium seals the seam between the top and bottom part of the cavity. The fundamental mode can be tuned by a $8 \times 8 \text{ mm}$ Aluminum plate attached to an Aluminum rod inserted from an opening in the cavity housing. The central position of the tuner at the strongest field strength allows a large tuning range from $\approx 9 \text{ GHz}$ to $\approx 7 \text{ GHz}$ by the 5 mm range of motion of an Attocube ANPz101 piezomechanical nanopositioner.

The cQED system is mounted on a gold-plated oxygen-free high-conductivity copper holder and surrounded by a μ -metal shield which protects it from static magnetic fields. Additionally, the magnetic shield of the lowest temperature stage of our Bluefors LD250 dilution refrigerator [5] is painted by an infrared absorptive material.

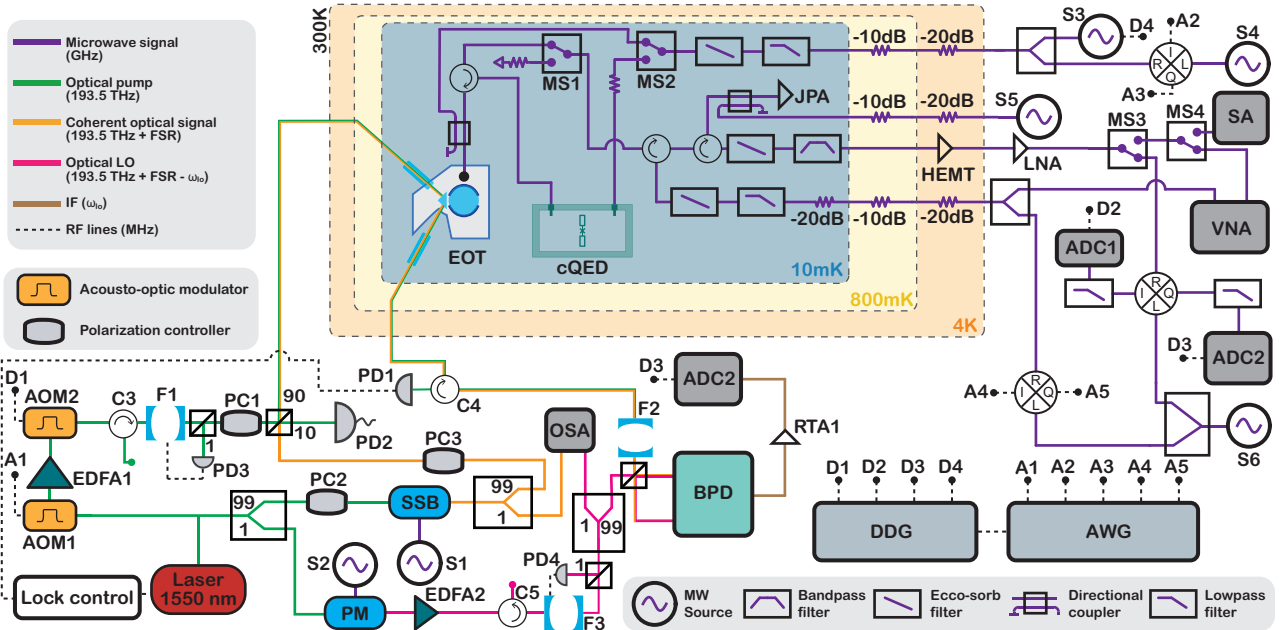
B. The electro-optic transceiver

The electro-optic device comprises an optical cavity by means of a LiNbO_3 whispering gallery mode (WGM) resonator and a cylindrical 3D cavity made of pure Aluminum. The center of the cavity exhibits circular protrusions from the cavity top and bottom forming a narrow, ring-shaped gap. As the rings clamp the optical resonator close the optical modes confined at the rim and additionally strongly confine the electric field of the $m = 1$ microwave resonance, the overlap between both fields is optimized. The microwave resonance can be tuned by roughly 500 MHz inserting an aluminum cylinder into the cavity by another Attocube piezomechanical nanopositioner. GRIN lenses focus the optical input and output from the optical fiber on a diamond prism coupled to the WGM resonator. More details about fabrication and characterization can be found in [6].

The device is identical to previous works [6–8] but suffered from an internal linewidth increase from $2\pi \times 7 \text{ MHz}$ to $\approx 2\pi \times 40 \text{ MHz}$. Together with with a reduced mode matching factor for the coupling between the single mode optical fiber to the electro-optic device, this results in an almost two orders of magnitude decrease in conversion efficiency. We attribute the linewidth broadening to damages in the LiNbO_3 disc induced by the clamping rings due to thermal expansion during warmup. A soft Indium clamping in the center of the disc far from the optical modes resolved this issue in a recent device and the optical linewidth remains constant during cooldown and warmup.

III. EXPERIMENT

The experimental setup is described in Supplementary Fig. 2 and the device parameters are listed in Supplementary Tab. 2.



Supplementary Fig. 2. **Experimental setup.** **Optical setup (bottom left)** A telecom laser (Toptica DLC CTL 1500) gets split into the optical pump (green) and the optical local oscillator (LO) for heterodyne detection (pink) respectively. The optical pump is amplified by an EDFA (Amonics AEDFA-PM-NS-200-10-23-M-FA) and pulse-shaped by two acousto-optical modulators (AOM, Fibre-Q T-M200-0.1C2J-3-F2P) with corresponding input signal from an arbitrary waveform generator (AWG, port A1, Spectrum Instrumentation M4i.6622-x8) and a digital delay/pulse generator (DDG, Stanford Research Systems DG645). An in-house filter cavity (F1) with analog PI-lock (PD3) removes the broadband noise from the EDFA amplification. The optical signal (orange) is generated by a single side-band modulator (SSB, Thorlabs DQPSK optical modulator) at the frequency of the Anti-Stokes mode, i.e. blue-shifted by 8.806 GHz. The optical LO (pink) is detuned from the laser frequency by a phase modulator (PM) and amplified. The PM's spurious modes are consequently cleaned by a tunable filter cavity (F3, MicronOptics FFPI) locked by software controlling a Peltier element. The optical output signal is cleaned from the reflected pump by another tunable filter (F2, MicronOptics FFPI) and finally combined with the optical LO for heterodyne detection on a balanced photodetector (Thorlabs PDB470). The downconverted signal is sent to an analog-digital converter (ADC2, port 2, AlazarTech ATS9870). **Microwave setup (top right)** An AWG (Quantum Machines OPX+) generates the qubit drive pulse via an IQ-mixer (ports A2, A3, Marki IQ-4509MXP). The pulse is sent either to the weakly coupled port of the qubit-cavity system (cQED system) or to the electro-optic transducer (EOT) for direct conversion measurements. The Quantum machines OPX+ also generates the qubit readout signal via an IQ-mixer (ports A4, A5, Marki IQ-0618MXP). The readout pulse is sent to the strongly coupled port of the cQED system. After being reflected there and at the EOT's microwave cavity, the pulse is routed via a reflective Josephson parametric amplifier [9], a cryogenic HEMT amplifier (Low Noise Factory LNF-LNC6_20C), and a room temperature low-noise amplifier (Agile AMT-A0067) to an IQ mixer. The downconverted signal from the IF port is sent to ADC2 (port 1) and the digitizer of Quantum Machines OPX+ (ADC1). Timing and synchronisation is controlled by the DDG. A vector network analyzer (VNA, Rohde and Schwartz ZVL13) can also be used to characterize the microwave setup. The microwave output or the signal from a 50 Ω termination (microwave switch MS1) may be sent to a spectrum analyzer (Rohde and Schwarz FSW26) for noise measurements. Further Acronyms: PC - polarization controller, PD - photodetector (Thorlabs PDA50B2, PDA05CF2, PDA20CS2)

Supplementary Tab. 2. **Device parameters.**

| Parameter | Symbol | Value |
|--|--------------------------|--|
| Qubit frequency | ω_q | $\omega_q/2\pi = 6.251\text{GHz}$ |
| Qubit-cavity coupling | g_{qc} | $g_{qc}/2\pi = 326\text{MHz}$ |
| Qubit anharmonicity | ν | $\nu/2\pi = 201\text{MHz}$ |
| Dispersive shift | χ | $\chi/2\pi = 6.6\text{MHz}$ |
| Cavity frequency | ω_c | $\omega_c/2\pi = 8.806\text{GHz}$ |
| Cavity linewidth | κ_c | $\kappa_c/2\pi = 1.4\text{MHz}$ |
| Weak port coupling | $\kappa_{c,w}$ | $\kappa_{c,w}/2\pi = 100\text{kHz}$ |
| Cavity internal loss | $\kappa_{c, \text{int}}$ | $\kappa_{c, \text{int}}/2\pi = 300\text{kHz}$ |
| Qubit lifetime | T_1 | $T_1 = 40\mu\text{s}$ |
| Ramsey time | T_2 | $T_2 = 1.5\mu\text{s}$ |
| Optical cavity frequency | ω_o | $\omega_o/2\pi = 193.4\text{THz}$ |
| Optical cavity external coupling | $\kappa_{o, \text{ext}}$ | $\kappa_{o, \text{ext}}/2\pi = 44\text{MHz}$ |
| Optical cavity linewidth | κ_o | $\kappa_o/2\pi = 81\text{MHz}$ |
| EO Microwave cavity frequency | ω_e | $\omega_e/2\pi = 8.806\text{GHz}$ |
| EO Microwave cavity external coupling rate | $\kappa_{e, \text{ext}}$ | $\kappa_{e, \text{ext}}/2\pi = 3.42\text{MHz}$ |
| EO Microwave cavity linewidth | κ_e | $\kappa_e/2\pi = 9.69\text{MHz}$ |
| Vacuum electro-optical coupling | g_{eo} | $g_{eo}/2\pi = 30\text{ Hz}$ |

-
- [1] M. D. Reed, L. DiCarlo, B. R. Johnson, L. Sun, D. I. Schuster, L. Frunzio, and R. J. Schoelkopf, *Phys. Rev. Lett.* **105**, 173601 (2010).
- [2] M. Boissonneault, J. M. Gambetta, and A. Blais, *Physical Review Letters* **105**, 100504 (2010).
- [3] L. S. Bishop, E. Ginossar, and S. M. Girvin, *Physical Review Letters* **105**, 100505 (2010).
- [4] C. W. Gardiner, *Physical Review Letters* **70**, 2269 (1993).
- [5] Bluefors LD Dilution Refrigerator Measurement System, <https://bluefors.com/products/dilution-refrigerator-measurement-systems/ld-dilution-refrigerator-measurement-system/>, accessed 23-10-2023.
- [6] W. Hease, A. Rueda, R. Sahu, M. Wulf, G. Arnold, H. G. Schwefel, and J. M. Fink, *PRX Quantum* **1**, 020315 (2020).
- [7] R. Sahu, W. Hease, A. Rueda, G. Arnold, L. Qiu, and J. M. Fink, *Nature Communications* **13**, 1276 (2022).
- [8] R. Sahu, L. Qiu, W. Hease, G. Arnold, Y. Minoguchi, P. Rabl, and J. M. Fink, *Science* **380**, 718 (2023).
- [9] P. Winkel, I. Takmakov, D. Rieger, L. Planat, W. Hasch-Guichard, L. Grünhaupt, N. Maleeva, F. Foroughi, F. Henriques, K. Borisov, J. Ferrero, A. V. Ustinov, W. Wernsdorfer, N. Roch, and I. M. Pop, *Physical Review Applied* **13**, 24015 (2020).